

PRINCIPLES OF TENSOR INDUCTION WELL LOGGING IN A DEVIATED WELL IN AN ANISOTROPIC MEDIUM

Michael S. Zhdanov*, W. David Kennedy, Arvidas B. Cheryauka, and Ertan Peksen
University of Utah and ExxonMobil Upstream Research Company

ABSTRACT

In this paper we develop an interpretation method for the characterization of conductivity anisotropy in an earth formation, based on the tensor induction well logging (TIWL) technique. The method is based on examining the response of a tri-axial electromagnetic induction logging instrument in a deviated well penetrating a transversely isotropic medium. The foundations of the TIWL method were developed in Zhdanov et al. (2001), where the low frequency approximations for the quadrature components of the induction tensor were derived. In this paper we further examine the basic principles of tensor induction logging in two-, three-, and multi-layer anisotropic formations in vertical and deviated wells using numerical simulation of tensor induction logs. We introduce a technique for correct reconstruction of the apparent conductivities of the anisotropic formations, based on application of a regularized Newton method. The method is fast and provides a “real time” interpretation. The practical effectiveness of this technique for tensor induction log interpretation is illustrated using results of numerical experiments.

INTRODUCTION

The identification of hydrocarbons and quantification of hydrocarbon pore volume in so-called “low resistivity pay” reservoirs has been a perennial problem for petrophysicists. More recently, the correct interpretation of resistivity logs in highly deviated and horizontal wells has challenged the petrophysicist’s understanding of resistivity instrument responses and reservoir resistivity distribution, particularly in anisotropic reservoirs. New resistivity instrumentation promises to mitigate or remove these difficulties.

We examine the response of a tri-axial electromagnetic induction logging instrument in a deviated well penetrating a transversely isotropic medium. The instrument responds to three mutually orthogonal components of magnetic field excited by each of three mutually orthogonal transmitters, the responses comprising a nine component induction tensor. Zhdanov et al. (2001) derived low frequency approximations for the quadrature components of the induction tensor by theoretically analyzing this tri-axial induction instrument for its response to magnetic field components induced in an infinite, homogeneous, anisotropic medium. The analysis

showed that the tensor components of conductivity and their orientation can be resolved from the quadrature components of the instrument response, providing a basic tensor logging instrument response interpretation. In this paper we further examine the basic principles of tensor induction logging in two-, three-, and multi-layer anisotropic formations in vertical and deviated wells using numerical simulations of tensor induction well logging (TIWL) data. We develop a technique for correct reconstruction of the apparent conductivities of the anisotropic formations, based on application of a regularized Newton method. We demonstrate the effectiveness of this technique for interpretation of tensor induction log data in a deviated well in an anisotropic medium. The method is fast and provides a “real time” interpretation.

PRINCIPLES OF TENSOR INDUCTION WELL LOGGING IN DEVIATED WELLS

Deviated wells and directional drilling are important in the oil industry. The main objective of this work is to study the TIWL response in a deviated well.

TIWL is based on analyses of the response of a tri-axial electromagnetic induction instrument in an anisotropic conductive medium. This instrument detects three components of the magnetic field due to each of three transmitters for a total of nine signals that are conveniently displayed as the components of a matrix

$$\hat{\mathbf{H}} = \begin{bmatrix} H_x^x & H_x^y & H_x^z \\ H_y^x & H_y^y & H_y^z \\ H_z^x & H_z^y & H_z^z \end{bmatrix},$$

R

where superscripts indicate the transmitter components and subscripts represent the receiver components.

In the Cartesian system of coordinates (x, y, z) , with the z axis directed along the axis of symmetry of the transversely isotropic (TI) conductive medium, the conductivity tensor can be represented by the diagonal matrix

$$\hat{\sigma} = \begin{bmatrix} \sigma_h & 0 & 0 \\ 0 & \sigma_h & 0 \\ 0 & 0 & \sigma_v \end{bmatrix},$$

where σ_h is the horizontal conductivity and σ_v is the vertical conductivity.

In this case, the expressions for the induction tensor components are written as (Zhdanov et al., 2001)

$$H_x^x = \frac{e^{ik_v s}}{4\pi} \left[\frac{k_h^2}{\lambda s} + \frac{ik_h s - k_h k_v x^2}{s\rho^2} - \frac{2ik_h x^2}{\rho^4} \right] - \frac{e^{ik_h r}}{4\pi} \left[\frac{ik_h r - k_h^2 x^2}{r\rho^2} - \frac{2ik_h x^2}{\rho^4} - \frac{ik_h}{r^2} + \frac{(k_h^2 x^2 + 1)}{r^3} + \frac{3ik_h x^2}{r^4} - \frac{3x^2}{r^5} \right], \quad (1)$$

$$H_y^x = H_x^y = xy \frac{e^{ik_v s}}{4\pi\rho^2} \left[-\frac{k_v k_h}{s} - \frac{2ik_h}{\rho^2} \right] - xy \frac{e^{ik_h r}}{4\pi} \left[-\frac{k_h^2}{r\rho^2} - \frac{2ik_h}{\rho^4} + \frac{k_h^2}{r^3} + \frac{3ik_h}{r^4} - \frac{3}{r^5} \right], \quad (2)$$

$$H_z^x = H_x^z = -xz \frac{e^{ik_h r}}{4\pi r^3} \left[k_h^2 + \frac{3ik_h}{r} - \frac{3}{r^2} \right], \quad (3)$$

$$H_y^y = \frac{e^{ik_v s}}{4\pi} \left[\frac{k_h^2}{\lambda s} + \frac{ik_h s - k_h k_v y^2}{s\rho^2} - \frac{2ik_h y^2}{\rho^4} \right] - \frac{e^{ik_h r}}{4\pi} \left[\frac{ik_h r - k_h^2 y^2}{r\rho^2} - \frac{2ik_h y^2}{\rho^4} - \frac{ik_h}{r^2} + \frac{(k_h^2 y^2 + 1)}{r^3} + \frac{3ik_h y^2}{r^4} - \frac{3y^2}{r^5} \right], \quad (4)$$

$$H_z^y = H_y^z = -yz \frac{e^{ik_h r}}{4\pi r^3} \left[k_h^2 + \frac{3ik_h}{r} - \frac{3}{r^2} \right], \quad (5)$$

$$H_z^z = \frac{e^{ik_h r}}{4\pi r} \cdot \left[k_h^2 + \frac{ik_h}{r} - \frac{(k_h^2 z^2 + 1)}{r^2} - \frac{3ik_h z^2}{r^3} + \frac{3z^2}{r^4} \right], \quad (6)$$

where the notations $\rho = \sqrt{x^2 + y^2}$, $s = \sqrt{\rho^2 + \lambda^2 z^2}$, $\lambda^2 = \sigma_h/\sigma_v$, $r = \sqrt{\rho^2 + z^2}$, $k_h^2 = i\omega\mu\sigma_h$, and $k_v^2 = i\omega\mu\sigma_v$ are used.

The magnetic field components are given in formulae (1)–(6) in a coordinate system defined by the horizontal and vertical principal axes of the transverse isotropic media. In practice, the orientation of the transmitter and receiver coils will be arbitrary with respect to this coordinate system. In order to use the representation of the field tensor $\hat{\mathbf{H}}$ for an instrument located in an arbitrary orientation with respect to the tensor principal axes, it is necessary

to transform the transmitter moment in the instrument frame (denoted by (x', y', z')) into the medium coordinates (denoted (x, y, z)). This transformation can be made by application of a rotation matrix.

The primed frame is related to the unprimed frame by two rotations about the origin. First, think of rotating z' around the y' axis through an angle α until z' coincides with z . After this rotation the x - y and x' - y' planes are co-planar. A further rotation around the z ($= z'$) axis through an angle β brings x and x' and y and y' into coincidence. The action of these rotations on a vector is mathematically represented by multiplication of vectors in the primed frame by a rotation matrix. The product gives the components of the vector in the medium, or unprimed, frame.

The rotation matrix $\hat{\mathbf{R}}$, as we discussed above, consists of two rotations

$$\hat{\mathbf{R}} = \hat{\mathbf{R}}_\alpha \hat{\mathbf{R}}_\beta,$$

where $\hat{\mathbf{R}}_\alpha$ describes the rotation around the y' axis

$$\hat{\mathbf{R}}_\alpha = \begin{bmatrix} \cos \alpha & 0 & -\sin \alpha \\ 0 & 1 & 0 \\ \sin \alpha & 0 & \cos \alpha \end{bmatrix},$$

and $\hat{\mathbf{R}}_\beta$ describes the rotation around the z ($= z'$) axis through an angle β ,

$$\hat{\mathbf{R}}_\beta = \begin{bmatrix} \cos \beta & \sin \beta & 0 \\ -\sin \beta & \cos \beta & 0 \\ 0 & 0 & 1 \end{bmatrix}.$$

The product of these two rotation matrices is given by

$$\hat{\mathbf{R}} = \hat{\mathbf{R}}_\beta \hat{\mathbf{R}}_\alpha = \begin{bmatrix} \cos \alpha \cos \beta & \cos \alpha \sin \beta & -\sin \alpha \\ -\sin \beta & \cos \beta & 0 \\ \sin \alpha \cos \beta & \sin \alpha \sin \beta & \cos \alpha \end{bmatrix}. \quad (7)$$

Represented in the coordinates defined by the conductivity tensor principal axes, the field is given in terms of its sources by

$$\hat{\mathbf{H}} = \hat{\mathbf{H}}\mathbf{M}. \quad (8)$$

Denoting the source moment by $\mathbf{M} = (M_x, M_y, M_z)^T$ when referring to the medium frame and by $\mathbf{M}' = (M'_x, M'_y, M'_z)^T$ when referring to the instrument frame, then the coordinate rotation $\hat{\mathbf{R}}$ transforms the field coordinates from the medium

frame to the instrument frame. For example, $\widehat{\mathbf{H}}' = \widehat{\mathbf{R}}\widehat{\mathbf{H}}$ and $\mathbf{M}' = \widehat{\mathbf{R}}\mathbf{M}$. Multiplication of the latter example from the left by $\widehat{\mathbf{R}}^{-1}$ gives

$$\mathbf{M} = \widehat{\mathbf{R}}^{-1}\mathbf{M}'. \quad (9)$$

Substituting (9) into (8), multiplying from the left by $\widehat{\mathbf{R}}$ and noting that $\widehat{\mathbf{H}}' = \widehat{\mathbf{R}}\widehat{\mathbf{H}}$, gives

$$\widehat{\mathbf{H}}' = \widehat{\mathbf{R}}\widehat{\mathbf{H}}\widehat{\mathbf{R}}^{-1}\mathbf{M}'. \quad (10)$$

This expresses the magnetic field in the instrument coordinate frame in terms of the source in the instrument coordinate frame and in terms of the magnetic induction tensor explicitly expressed in the medium coordinate frame. We note that, with the definition

$$\widehat{\mathbf{H}}' \equiv \widehat{\mathbf{R}}\widehat{\mathbf{H}}\widehat{\mathbf{R}}^{-1} = \widehat{\mathbf{R}}\widehat{\mathbf{H}}\widehat{\mathbf{R}}^T, \quad (11)$$

the field equations in the instrument frame have a form identical to their form in the medium frame; i.e.,

$$\widehat{\mathbf{H}}' = \widehat{\mathbf{H}}'\mathbf{M}', \quad (12)$$

where $\widehat{\mathbf{H}}'$ is the representation of the induction tensor in the instrument frame. The components of $\widehat{\mathbf{H}}'$ are used in the estimation of receiver voltages.

APPARENT CONDUCTIVITIES BASED ON LOW FREQUENCY ASYMPTOTICS

The analysis of the low frequency asymptotics of the expressions (1)–(6) helped develop the following formulae for the low frequency “horizontal” apparent conductivity, σ_{ha}^0 , apparent anisotropy coefficient, λ_a^0 , and apparent dip angle, α_a^0 , calculations (Zhdanov et al., 2001):

$$\sigma_{ha}^0 = \frac{1}{2g_0} \left[\text{Im}H_{x'}^{x'} + \frac{1}{2}\text{Im}H_{z'}^{z'} + \sqrt{\left(\text{Im}H_{x'}^{x'} - \frac{1}{2}\text{Im}H_{z'}^{z'} \right)^2 + 2\text{Im}^2 H_{z'}^{x'}} \right], \quad (13)$$

$$\lambda_a^0 = \frac{4g_0^2\sigma_{ha}^2}{\text{Im}H_{z'}^{z'}} \frac{1}{\left(\text{Im}H_{y'}^{y'} + \text{Im}H_{x'}^{x'} + \text{Im}H_{z'}^{z'} - 2g_0\sigma_{ha} \right)}, \quad (14)$$

and

$$\alpha_a^0 = \frac{1}{2} \sin^{-1} \left[\frac{2\text{Im}H_{z'}^{x'}}{\text{Im}H_{x'}^{x'} + \text{Im}H_{z'}^{z'} - 3g_0\sigma_{ha}^0} \right], \quad (15)$$

where Im is the imaginary part of the magnetic field component; $H_{x'}^{x'}$, $H_{y'}^{y'}$, $H_{z'}^{z'}$, and $H_{z'}^{x'}$ are the magnetic field components in the instrument coordinate system; g_0 is a constant given by

$$g_0 = \frac{\omega\mu_0}{8\pi L},$$

where ω is the angular frequency, μ_0 is the free-space magnetic permeability, and L is a transmitter-receiver separation.

The expression for the “vertical” apparent conductivity, σ_{va}^0 , has the form

$$\sigma_{va}^0 = \frac{\sigma_{ha}^0}{(\lambda_a^0)^2}. \quad (16)$$

For a vertically oriented tool, the expression for the apparent horizontal conductivity coincides with the traditional expression for the apparent conductivity in isotropic media,

$$\sigma_{ha}^0 = \frac{4\pi L}{\omega\mu_0} \text{Im}H_z^{z0}, \quad (17)$$

which is called “conventional apparent conductivity”. In this special case, the expression for the vertical apparent conductivity calculation is (Zhdanov et al., 2001)

$$\sigma_{va}^0 = \frac{8\pi L}{\omega\mu_0} \text{Im}H_x^{x0}. \quad (18)$$

In formulae (17) and (18), H_z^{z0} and H_x^{x0} are the magnetic field components for the vertically oriented tool. The exact formulae for these components can be obtained from the general expressions (6) and (1) by evaluating the last formulae in the limit $\rho \rightarrow 0$. In this case $s \rightarrow \lambda L$, $r \rightarrow L$, $z = L$, and

$$H_z^{z0} = \frac{e^{ik_h L}}{2\pi L^3} (1 - ik_h L), \quad (19)$$

$$H_x^{x0} = -\frac{e^{ik_h L}}{4\pi L^3} \left[1 - ik_h L - \frac{1 + \lambda^2}{2\lambda^2} k_h^2 L^2 \right]. \quad (20)$$

Thus, the TIWL method consists in measuring the components of the magnetic induction tensor by a tri-axial induction instrument and computing the apparent conductivities using formulae (13) and

R

(16). These formulae are based on the low frequency asymptotics of field components (1)–(6). Therefore, these apparent conductivities provide only an approximate estimate for the real conductivities of anisotropic media. In order to obtain more accurate parameter estimates for the medium, we can use a simple inversion scheme based on the exact expression of the induction tensor components. We discuss this technique in the next section.

REGULARIZED NEWTON METHOD FOR INTERPRETATION OF TIWL DATA

In this section, we develop a technique for calculating the tensor induction well logging apparent conductivities using the rigorous solutions for the homogeneous anisotropic media (1)–(6). Our technique is based on inversion of the tensor induction log data for the parameters of the equivalent homogeneous anisotropic media using a regularized Newton method. We will illustrate this method for an arbitrary induction array orientation. The expressions for the magnetic field components in homogeneous anisotropic media in the instrument coordinate system can be obtained from the corresponding formulae (1)–(6), developed in the medium coordinate system, by application of the rotational transformation (11).

The algorithm of the regularized Newton method is described by Zhdanov (1993). If n is the iteration index

$$\mathbf{r}_n = \mathbf{A}(\mathbf{m}_n) - \mathbf{d}, \quad (21)$$

$$\mathbf{I}_n^{\nu_n} = \mathbf{I}^{\nu_n}(\mathbf{m}_n) = \mathbf{F}_{\mathbf{m}_n}^T \mathbf{r}_n + \nu_n(\mathbf{m} - \mathbf{m}_{apr}), \quad (22)$$

$$\mathbf{H}_{\mathbf{m}_n} = \mathbf{F}_{\mathbf{m}_n}^T \mathbf{F}_{\mathbf{m}_n} + \nu_n \mathbf{I}, \quad (23)$$

$$\mathbf{m}_{n+1} = \mathbf{m}_n - \mathbf{H}_{\mathbf{m}_n}^{-1} \mathbf{I}_n^{\nu_n} \quad (24)$$

where \mathbf{A} is a nonlinear operator of the forward modeling described by formulae (1)–(6) and (12); \mathbf{d} is a vector of observed data, \mathbf{m}_n is a vector of model parameters (horizontal and vertical conductivities, σ_h and σ_v , and the dip angle α) on the n -th iteration, \mathbf{m}_{apr} is the a priori model, \mathbf{r} is a residual vector of the difference between the predicted, $\mathbf{A}(\mathbf{m}_n)$, and observed data; $\mathbf{F}_{\mathbf{m}_n}$ is a Frechet derivative matrix; $\mathbf{H}_{\mathbf{m}_n}^{-1} = (\mathbf{F}_{\mathbf{m}_n}^* \mathbf{F}_{\mathbf{m}_n})^{-1}$ is a quasi Hessian matrix; $\mathbf{I}_n^{\nu_n}$ is the regularized direction of a Newton method on the n -th iteration (Zhdanov, 1993).

The regularization parameter ν is updated on each iteration according to a progression of numbers

$$\nu_k = \nu_0 q^k; \quad k = 0, 1, 2, \dots, n; \quad (25)$$

where coefficient q determines the rate of decreasing ν_k : $0 < q < 1$. The first iteration of the Newton method is run with $\nu = 0$. The initial value of the regularization parameter, ν_0 , is determined after the first iteration, \mathbf{m}_1 , as the ratio

$$\nu_0 = \frac{\|\mathbf{A}(\mathbf{m}_1) - \mathbf{d}\|^2}{\|\mathbf{m}_1 - \mathbf{m}_{apr}\|^2}.$$

For any number ν_k we calculate the misfit $\|\mathbf{A}(\mathbf{m}_{\nu_k}) - \mathbf{d}\|^2$. The optimal value of the parameter ν is the number ν_{k0} , for which we have satisfied the misfit condition,

$$\|\mathbf{A}(\mathbf{m}_{\nu_{k0}}) - \mathbf{d}\|^2 = \delta, \quad (26)$$

where δ is the level of noise in the observed data.

There are three unknown model parameters; i.e., the dip angle α and the horizontal and vertical conductivities, σ_h and σ_v . Therefore, the Frechet derivative matrix can be calculated directly by taking derivatives of expressions (1)–(6) and (12), with respect to unknown parameters. The matrix is

$$\mathbf{F} = \begin{bmatrix} \frac{\partial H_x'}{\partial \sigma_h} & \frac{\partial H_x'}{\partial \sigma_v} & \frac{\partial H_x'}{\partial \alpha} \\ \frac{\partial H_z'}{\partial \sigma_h} & \frac{\partial H_z'}{\partial \sigma_v} & \frac{\partial H_z'}{\partial \alpha} \\ \frac{\partial H_y'}{\partial \sigma_h} & \frac{\partial H_y'}{\partial \sigma_v} & \frac{\partial H_y'}{\partial \alpha} \\ \frac{\partial H_x''}{\partial \sigma_h} & \frac{\partial H_x''}{\partial \sigma_v} & \frac{\partial H_x''}{\partial \alpha} \\ \frac{\partial H_z''}{\partial \sigma_h} & \frac{\partial H_z''}{\partial \sigma_v} & \frac{\partial H_z''}{\partial \alpha} \end{bmatrix}. \quad (27)$$

In the Newton algorithm the calculations start with an initial guess, which is usually set equal to the a priori model, $\mathbf{m}_0 = \mathbf{m}_{apr}$, and then update it on each iteration according to (24). The method is fast and usually converges after 4–to–6 iterations.

The correct choice of the initial guess is vital for the Newton method. If the algorithm starts with the initial guesses, that are “far” from the true solution, the Newton method may not converge. Fortunately, in our case, we select a starting model that is often very close to the true solutions. The initial model parameters are based on the low frequency apparent conductivities, σ_{ha}^0 and σ_{va}^0 , and apparent anisotropy coefficient λ_a^0 , introduced above by expressions (13), (16), and (14).

The regularized Newton routine solves for three parameters at each TIWL observation point. These parameters are the horizontal and vertical conductivities, and the dip angle.

NUMERICAL EXAMPLES

In the model study, we examined the basic principles of the TIWL method using numerical simula-

tion. We considered the simplest case of a layered model of rock formation without a borehole and invaded zones. The tensor induction tool has three mutually orthogonal transmitters and three mutually orthogonal receivers, with the “vertical” transmitter and receiver oriented along the deviated borehole. The distance between the transmitter’s position and the receiver’s position was 1.0 m. The calculations were performed for a tool moving along a borehole, sampled every 0.25 m. The operating frequency was 20 kHz.

The synthetic data were computed using a library of 3-D Green’s tensors in layered anisotropic formations (Cheryauka and Zhdanov, 2001a). The forward response for a layered model can be calculated using Green’s functions. After computing the Green’s tensor components, the magnetic fields may be found as

$$\hat{\mathbf{H}} = i\omega\mu_0\hat{\mathbf{G}}^{\text{H}}, \quad (28)$$

where $\hat{\mathbf{G}}^{\text{H}}$ is the Green’s tensor for a layered model

$$\hat{\mathbf{G}}^{\text{H}} = \begin{bmatrix} G_x^x & G_x^y & G_x^z \\ G_y^x & G_y^y & G_y^z \\ G_z^x & G_z^y & G_z^z \end{bmatrix}.$$

The response of the layered anisotropic model was calculated in the model coordinate system. The result then was transformed from the model frame to the instrument frame, using a rotation matrix.

Two-layer model with a dip angle We assume that tensor induction logging is conducted by a tool coaxial with a borehole. We calculate the model responses (induction tensor components) for the different positions of the tool along the borehole. Using these responses as the synthetic data, we compute the low frequency (σ_{ha}^0 and σ_{va}^0) apparent conductivities according to formulae (13) and (16) as an initial model. Then more accurate estimations of the apparent conductivities, σ_{ha} and σ_{va} , were computed using the Newton inversion, as described in the previous section. The results were plotted as apparent resistivity curves, ρ_{ha}^0 , ρ_{va}^0 , ρ_{ha} , and ρ_{va} , versus depth for a different dip angle α , equal to 0, 30, 60, and 85 degrees, respectively (Figures 1–4).

Each of the Figures (1–4) has four panels. The first panel on the left shows the parameters of the two layer model. The second two panels present the apparent resistivity curves versus depth. The last panel displays the apparent anisotropy coefficient values versus depth. The solid lines show the true parameters of the model. The apparent resistivities

and anisotropy coefficient, ρ_{ha}^0 , ρ_{va}^0 , and λ_a^0 , obtained by the low frequency asymptotics, are shown by the dotted lines. The circles represent the inverted apparent resistivities and anisotropy coefficient, ρ_{ha} , ρ_{va} , and λ_a .

The data were contaminated by 3% random Gaussian noise at each observation point. One can see that the low frequency asymptotics overestimates the vertical resistivities and the anisotropy coefficient for dip angle values below 45 degrees. At α equal to 60 degrees, the apparent parameters are surprisingly close to the true model. At the larger dip angle ($\alpha = 85$ degrees) the low frequency asymptotics underestimate the vertical resistivities and the anisotropy coefficient. At the same time, the apparent parameters inverted by use of the regularized Newton method are very close to the true parameters of the model for any dip angle (the curves shown by circles in Figures 1–4).

Note that in this model, with the conventional induction tool, we can obtain only one apparent conductivity, which reflects the integrated effect of both vertical and horizontal conductivities.

The boundary cannot be seen by using only the apparent resistivity expression for ρ_{ha} (Figure 1). But the vertical apparent resistivity clearly responds to the position of the boundary. The ρ_{va} curve changes sharply when the tool reaches the boundary. This model provides a simple illustration of an important additional power of tensor induction well logging in anisotropic formation in comparison with the traditional induction logging tool.

Three-layer model with a dip angle In the next set of numerical simulations, we consider a model of a three-layer formation. Figure 5 shows the model on the left panel. This model is a very good example of a practical situation where conventional induction logging can miss a geological structure. The layer thickness is 5m. There is no horizontal conductivity variation in this model, while the vertical conductivity of the second layer is different from the top and bottom layers. On the second panel from the left, representing the horizontal apparent resistivities, we cannot see any indication of the second layer. However, it is possible to determine the layer boundaries by using vertical resistivity information (the third panel from the left). The last panel displays the anisotropy coefficient values versus depth.

The synthetic data simulated for this model were contaminated by 3% random Gaussian noise. The solid lines show the true parameters of the model.

R

The apparent resistivities and anisotropy coefficient, ρ_{ha}^0 , ρ_{va}^0 , and λ_a^0 , obtained by low frequency asymptotics, are shown by the dotted lines. The circles represent the inverted apparent resistivities ρ_{ha} , ρ_{va} , and anisotropy coefficient, λ_a , computed using the regularized Newton method. Figure 5 presents the TIWL data interpretation results for a case of a vertical well (the dip angle α is equal to 0). Figures 6–8 show similar results for the different dip angles 30, 60, and 85 degrees, respectively. One can observe the same regularity in these plots as in Figures 1–4. The low frequency asymptotics overestimates the vertical resistivities and the anisotropy coefficient for dip angle values below 45 degrees, and underestimates these parameters for a dip angle above 60 degrees. The inversion of TIWL data, based on the Newton method, provides practically correct reconstruction of the true parameters of the model within the entire range of dip angles (the curves shown by circles in Figures 5–8).

Multi-layer models of anisotropic formations with a dip angle

We considered three multi-layered models of anisotropic formations, based on the well known benchmark models: Anderson and Barber (1999) model, “Oklahoma” model, and “Chirp” model. The first one is a modified model, considered by Anderson and Barber (1999, p.135, Figure 3). The horizontal resistivity profile of our model is the same as in Anderson and Barber (1999). It is shown by the solid line in the left panel of Figure 9. We introduced the anisotropic layers in this model with the vertical resistivity shown by the solid lines in the right panel of Figure 9. We simulated the synthetic data for this model using a library of 3-D Green’s tensors in the layered anisotropic formations (Cheryauka and Zhdanov, 2001a). The data were contaminated by 3% random Gaussian noise. Figure 9 presents the TIWL data interpretation results for the case of a vertical well (the dip angle α is equal to 0). Figure 10 presents similar results for the dip angle of 30 degrees. The solid lines show the true parameters of the model. The apparent resistivities and anisotropy coefficient, ρ_{ha}^0 , ρ_{va}^0 , and λ_a^0 , obtained by the low frequency asymptotics, are shown by the dotted lines. The circles represent the inverted apparent resistivities ρ_{ha} , ρ_{va} , and anisotropy coefficient, λ_a , computed using the Newton method.

The second multi-layered model is the “Oklahoma” model (Barber et al., 1999). In our anisotropic model we use the same horizontal resistivity as in the original “Oklahoma” model (solid

line in the left panel of Figure 11) but we also add some anisotropy to the model by assigning various vertical resistivities (solid line in the right panel of Figure 11). The computer simulated data for this model with 3% random noise added were processed using the TIWL interpretation technique outlined above. The results of interpretation for the dip angles of 0 and of 30 degrees are presented in Figure 11 and 12. One can see that we can reconstruct well the horizontal resistivity distribution, while the vertical resistivity is mostly underestimated in this case.

The third model is the “Chirp” model (Fang and Wang, 2000), represented by a solid line in the left panel of Figure 13 (the horizontal resistivity profile). We modified this model, adding a profile of vertical resistivity (right panel in Figure 13). The results of the synthetic TIWL data interpretation for different dip angles are shown in Figures 13–14. Once again the apparent resistivities describe well the horizontal resistivity, but recover the vertical resistivity much less successfully. These results show that, in the case of complicated geoelectrical models, the simple interpretation tool based on the apparent resistivity model cannot well resolve the different anisotropic layers. In this case one should use more advanced technology based on multilayered inversion. Some elements of this development are discussed in the paper by Cheryauka and Zhdanov (2001b).

CONCLUSIONS

In this paper we examined the basic principles of tensor induction well logging (TIWL) in the deviated borehole in anisotropic layered formations. We introduced a simple technique of TIWL data interpretation based on calculating the components of the apparent conductivity tensor (“horizontal” and “vertical” apparent conductivity). In the case of low frequency asymptotics, we can use the analytical expressions for apparent conductivity (or resistivity) tensor calculations. In the higher frequency range, one can use a regularized Newton method to generate the corresponding apparent conductivities (or resistivities) of the anisotropic media.

We analyzed the responses of synthetic tensor induction logs in the deviated borehole through two-, three-, and multi-layer anisotropic formations in vertical and deviated wells using numerical simulation. Our results demonstrate that the tensor instrument is sensitive to anisotropic parameters of geological formations. These cannot be detected in a general case by conventional induction logging.

At the same time, we found that the simple interpretation tool based on the apparent resistivity model cannot well resolve the different anisotropic layers in the case of the complicated geoelectrical models. There is a need to develop a more advanced technology for TIWL data interpretation based on multilayered inversion.

ACKNOWLEDGMENTS

The authors acknowledge the support of the University of Utah Consortium for Electromagnetic Modeling and Inversion (CEMI), which includes AGIP, Baker Atlas Logging Services, BHP Minerals, ExxonMobil Upstream Research Company, INCO Exploration, International Energy Services, Japan National Oil Corporation, MINDECO, Naval Research Laboratory, Rio Tinto-Kennecott, Sumitomo Metal Mining Co., and 3JTech Corporation.

REFERENCES

- Anderson, B. and T. D. Barber, 1999, Deconvolution and boosting parameters for obsolete Schlumberger induction tools: *The Log Analyst*, **40**, No 2 (March-April), 133-137.
- Barber, T. D., Broussard, T., Minerbo, G. N. Sijeric, Z. and D. Murgatroyd, 1999, Interpretation of multiarray induction logs in invaded formations at high relative dip angles: *The Log Analyst*, **40**, No 3 (May-June), 202 - 217.
- Fang, S., and T. Wang, 2000, Accurate Born simulation of induction response using an optimal background: SEG 2000 Expanded Abstracts, Calgary, 1806-1809.
- Cheryauka, A. and M. S. Zhdanov, 2001a, Electromagnetic tensor Green's functions in transverse isotropic layered media: *IEEE Transactions on Geoscience and Remote Sensing*, in submission.
- Cheryauka, A. and M. S. Zhdanov, 2001b, Focusing inversion of tensor induction logging data in a deviated well in layered anisotropic formations: *Petrophysics*, in submission.
- Zhdanov, M. S., 1993, Tutorial: Regularization in inversion theory; Colorado School of Mines, Golden, Colorado, CWP-136,47pp.
- Zhdanov, M. S., Kennedy, D., and E. Peksen, 2001, Foundations of tensor induction well logging: *Petrophysics*, in press.

ABOUT THE AUTHORS

Michael S. Zhdanov joined the University of Utah as a full professor in 1993. He has been Director of the Consortium for Electromagnetic Modeling and Inversion since 1995. He received a Ph.D. in 1970 from Moscow State University. He spent more than twenty years as a professor at the Moscow Academy of Oil and Gas, and as the head of the Department of Deep Electromagnetic Study and as Deputy Director of IZMIRAN, and later as Director of the Geoelectromagnetic Research Institute of the United Institute of Physics of the Earth, Russian Academy of Science, Moscow, Russia, before moving to the University of Utah. In 1990 he was awarded an Honorary Diploma of Gauss Professorship by the Gottingen Academy of Sciences, Germany. In 1991 he was elected Full Member of the Russian Academy of Natural Sciences. He became Honorary Professor of the China National Center of Geological Exploration Technology in 1997.

W. David Kennedy See biography in *Petrophysics*, volume 42, no 2, 2001.

Arvidas B. Cheryauka received his M.Sc. in Geophysics from the Novosibirsk State University, Russia in 1986 and a Ph.D in Geophysics from Institute for Geophysics, Siberian Branch of Russian Academy of Sciences in 1989. From 1995-1998 he worked as a consultant for LOOCH Geophysical Engineering and Baker Atlas companies. During 1998-1999, Arvidas was a visiting scientist with Tohoku University in Sendai, Japan. Since 1999 he has been working as a research scientist with Consortium for Electromagnetic Modeling and Inversion, University of Utah on the development of new array technologies for subsurface and well-logging sensing.

Ertan Peksen is a PhD student at the Consortium for Electromagnetic Modeling and Inversion, the University of Utah. He graduated in 1993 (BS) from the University of Ankara, in geophysics. He received his Master of Science degree in geophysics from the Department of Geology and Geophysics, the University of Utah, in 1999. His research interest is modeling and inversion of tensor induction well logging in anisotropic media.

R

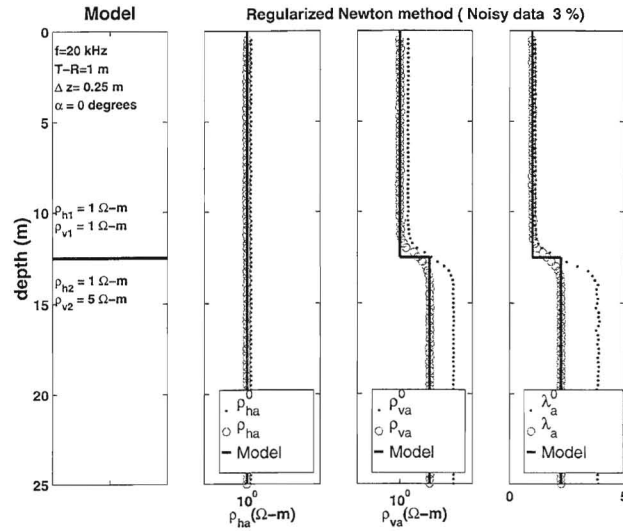


Figure 1: The first panel on the left shows a two-layer anisotropic model with resistivities $\rho_{h1} = 1\Omega\text{m}$, $\rho_{v1} = 1\Omega\text{m}$, $\rho_{h2} = 1\Omega\text{m}$, and $\rho_{v2} = 5\Omega\text{m}$. The second and third panels present the apparent resistivity curves versus depth. The last panel displays the apparent anisotropy coefficient values. Data are contaminated by 3 % random noise. The dip angle is 0° .

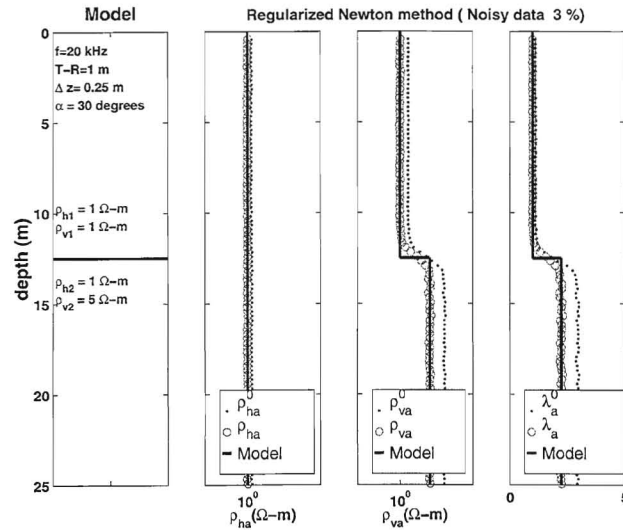


Figure 2: The first panel on the left shows a two-layer anisotropic model with resistivities $\rho_{h1} = 1\Omega\text{m}$, $\rho_{v1} = 1\Omega\text{m}$, $\rho_{h2} = 1\Omega\text{m}$, and $\rho_{v2} = 5\Omega\text{m}$. The second and third panels present the apparent resistivity curves versus depth. The last panel displays the apparent anisotropy coefficient values. Data are contaminated by 3 % random noise. The dip angle is 30° .

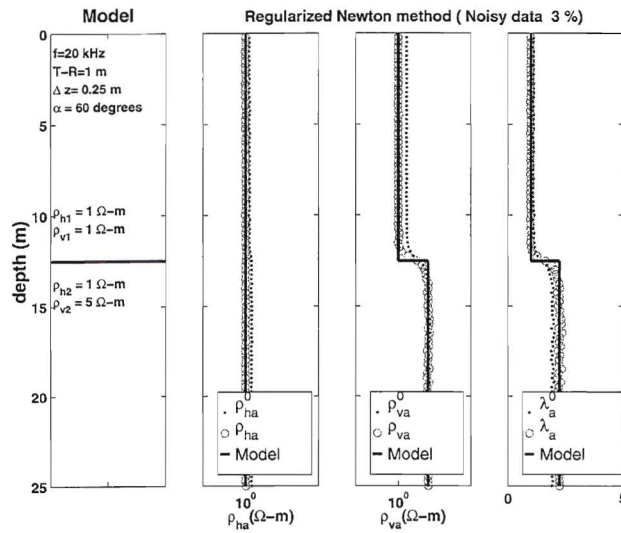


Figure 3: The first panel on the left shows a two-layer anisotropic model with resistivities $\rho_{h1} = 1\Omega\text{m}$, $\rho_{v1} = 1\Omega\text{m}$, $\rho_{h2} = 1\Omega\text{m}$, and $\rho_{v2} = 5\Omega\text{m}$. The second and third panels present the apparent resistivity curves versus depth. The last panel displays the apparent anisotropy coefficient values. Data are contaminated by 3 % random noise. The dip angle is 60° .

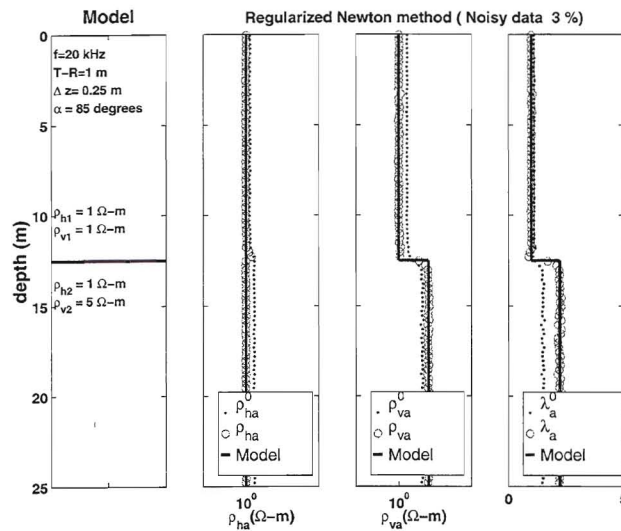


Figure 4: The first panel on the left shows a two-layer anisotropic model with resistivity $\rho_{h1} = 1\Omega\text{m}$, $\rho_{v1} = 1\Omega\text{m}$, $\rho_{h2} = 1\Omega\text{m}$, and $\rho_{v2} = 5\Omega\text{m}$. The second and third panels present the apparent resistivity curves versus depth. The last panel displays the apparent anisotropy coefficient values. Data are contaminated by 3 % random noise. The dip angle is 85° .

R

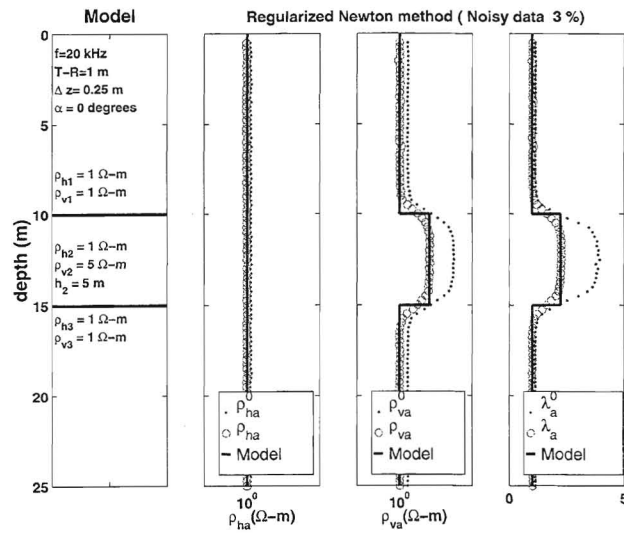


Figure 5: The first panel on the left shows a three-layer anisotropic model. The thickness of the pay zone is 5m with the resistivities $\rho_{h2} = 1\Omega m$, and $\rho_{v2} = 5\Omega m$. The second and third panels present the apparent resistivity curves versus depth. The last panel displays the apparent anisotropy coefficient values. Data are contaminated by 3 % random noise. The dip angle is 0^0 .

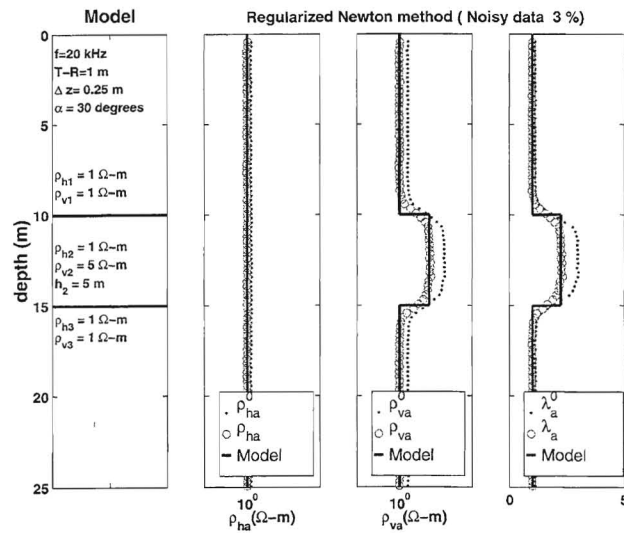


Figure 6: The first panel on the left shows a three-layer anisotropic model. The thickness of the pay zone is 5m with the resistivities $\rho_{h2} = 1\Omega m$, and $\rho_{v2} = 5\Omega m$. The second and third panels present the apparent resistivity curves versus depth. The last panel displays the apparent anisotropy coefficient values. Data are contaminated by 3 % random noise. The dip angle is 30^0 .

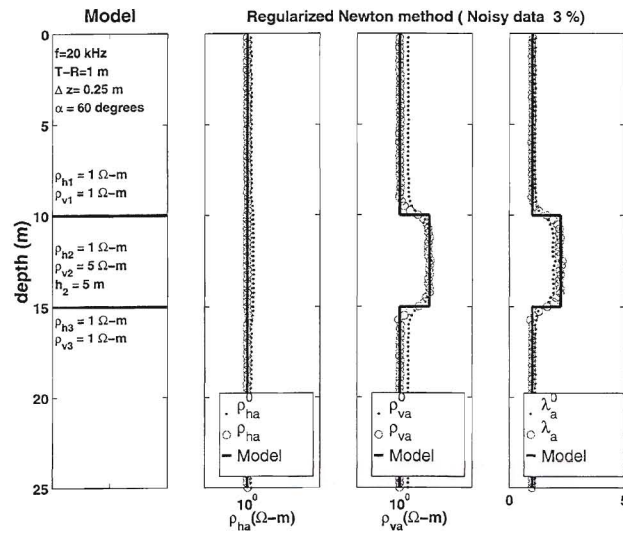


Figure 7: The first panel on the left shows a three-layer anisotropic model. The thickness of the pay zone is 5m with the resistivities $\rho_{h2} = 1\Omega\text{m}$, and $\rho_{v2} = 5\Omega\text{m}$. The second and third panels present the apparent resistivity curves versus depth. The last panel displays the apparent anisotropy coefficient values. Data are contaminated by 3% random noise. The dip angle is 60° .

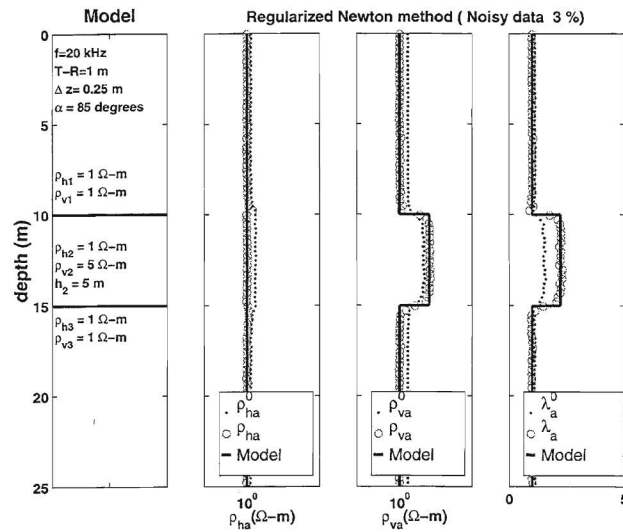


Figure 8: The first panel on the left shows a three-layer anisotropic model. The thickness of the pay zone is 5m with the resistivities $\rho_{h2} = 1\Omega\text{m}$, and $\rho_{v2} = 5\Omega\text{m}$. The second and third panels present the apparent resistivity curves versus depth. The last panel displays the apparent anisotropy coefficient values. Data are contaminated by 3% random noise. The dip angle is 85° .

R

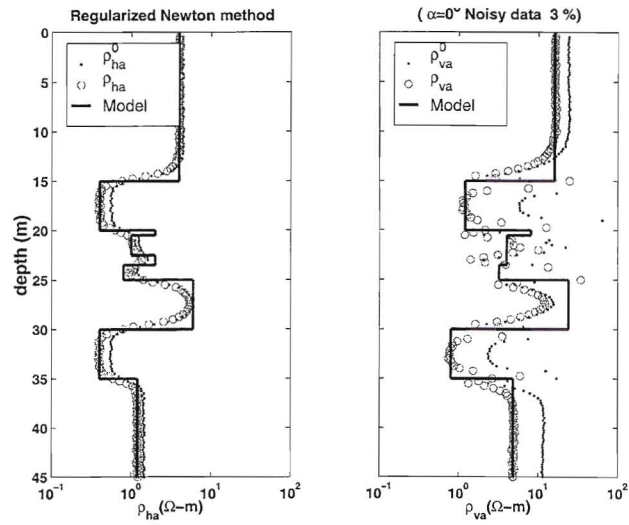


Figure 9: Multi-layer model of anisotropic formation. The left panel shows the apparent horizontal resistivities versus depth, and the right one illustrates the apparent vertical resistivities versus depth. Data are contaminated by 3 % random noise. The dip angle is 0° .

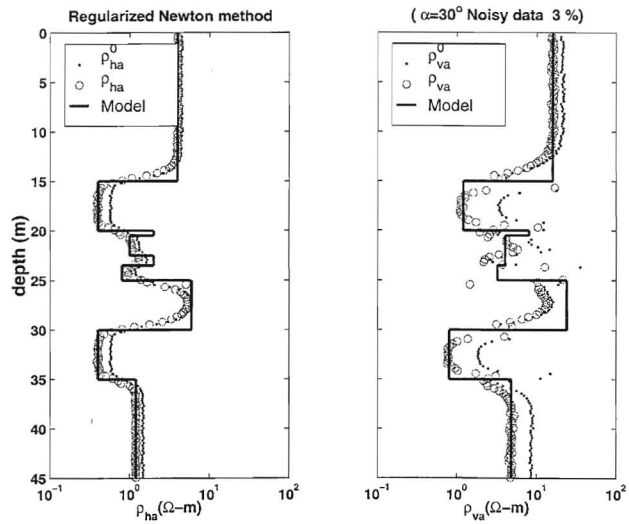


Figure 10: Multi-layer model of anisotropic formation. The left panel shows the apparent horizontal resistivities versus depth, and the right one illustrates the apparent vertical resistivities versus depth. Data are contaminated by 3 % random noise. The dip angle is 30° .

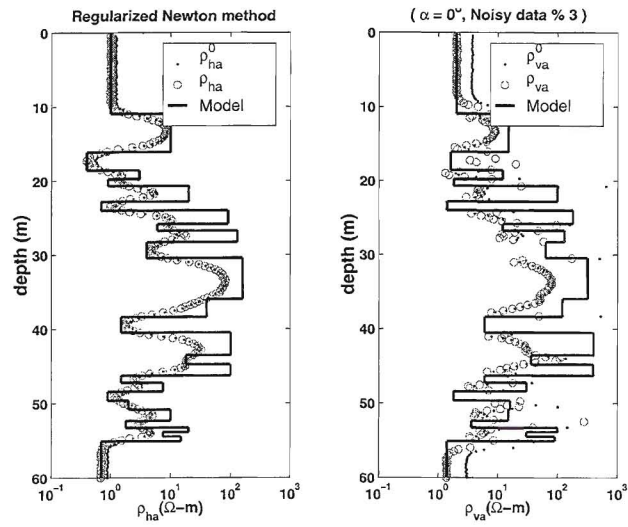


Figure 11: Multi-layer model of anisotropic formation (Oklahoma-like model). The left panel shows the apparent horizontal resistivities versus depth, and the right one illustrates the apparent vertical resistivities versus depth. Data are contaminated by 3 % random noise. The dip angle is 0° .

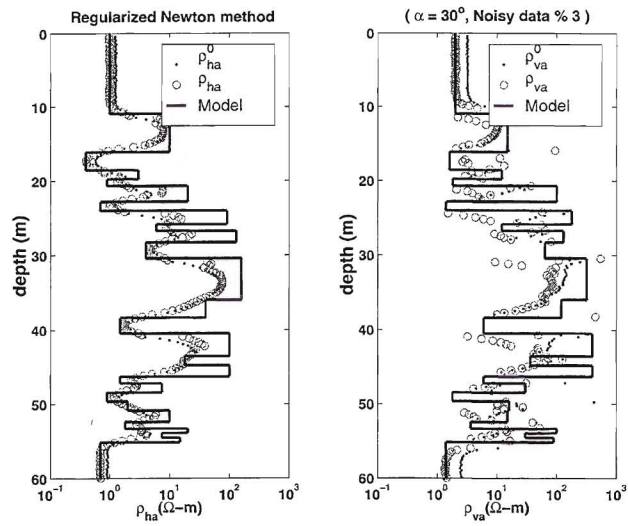


Figure 12: Multi-layer model of anisotropic formation (Oklahoma-like model). The left panel shows the apparent horizontal resistivities versus depth, and the right one illustrates the apparent vertical resistivities versus depth. Data are contaminated by 3 % random noise. The dip angle is 30° .

R

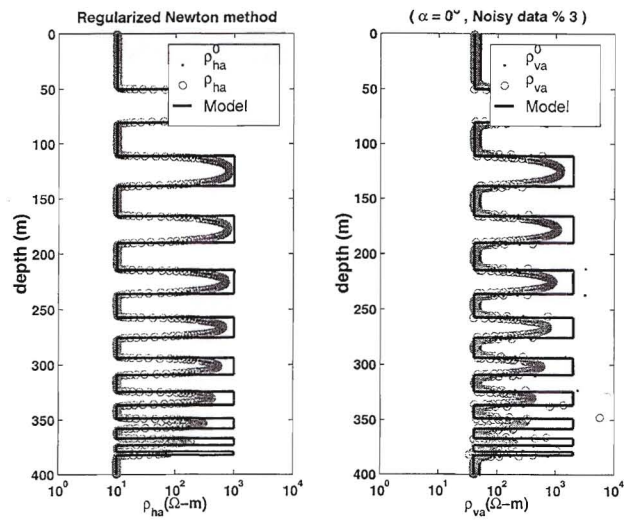


Figure 13: Multi-layer model of anisotropic formation (Chirp-like model). The left panel shows the apparent horizontal resistivities versus depth, and the right one illustrates the apparent vertical resistivities versus depth. Data are contaminated by 3 % random noise. The dip angle is 0° .

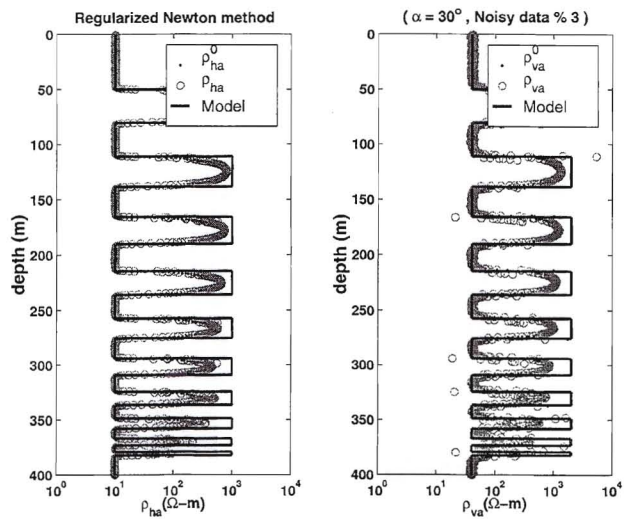


Figure 14: Multi-layer model of anisotropic formation (Chirp-like model). The left panel shows the apparent horizontal resistivities versus depth, and the right one illustrates the apparent vertical resistivities versus depth. Data are contaminated by 3 % random noise. The dip angle is 30° .